MOLECULAR IMAGING AND BIOLOGY

Mol Imaging Biol (2019) 21:149–158
DOI: 10.1007/s11307-018-1205-z

RESEARCH ARTICLE

Zero-Extra-Dose PET Delayed Imaging with Data-Driven Attenuation Correction Estimation

Lifang Pang,[1,2,3] Wentao Zhu,[4] Yun Dong,[5] Yang Lv,[5] Hongcheng Shi[1,2,3]

[1]*Department of Nuclear Medicine, Zhongshan Hospital, Fudan University, No. 180, Fenglin Road, Shanghai, 200032, People's Republic of China*
[2]*Shanghai Institute of Medical Imaging, Shanghai, 200032, China*
[3]*Institute of Nuclear Medicine, Fudan University, Shanghai, 200032, China*
[4]*UIH America, Inc, 9230 Kirby Dr, Suite 600, Houston, TX, 77054, USA*
[5]*Shanghai United Imaging Healthcare Co., Ltd, 2258 Chengbei Rd, Jiading District, Shanghai, 201807, China*

Abstract

Purpose: Delayed positron emission tomography (PET) imaging may improve sensitivity and specificity in lesion detection. We proposed a PET data-driven method to estimate the attenuation map (AM) for the delayed scan without an additional x-ray computed tomography (CT).

Procedures: An emission-attenuation-scatter joint estimation framework was developed. Several practical issues for clinical datasets were addressed. Particularly, the unknown scatter correction was incorporated in the joint estimation algorithm. The scaling problem was solved using prior information from the early CT scan. Fourteen patient datasets were added to evaluate the method. These patients went through two separate PET/CT scans. The delayed CT-based AM served as ground truth for the delayed scan. Standard uptake values (SUVmean and SUVmax) of lesion and normal tissue regions of interests (ROIs) in the early and delayed phase and the respective %DSUV (percentage change of SUVmean at two different time points) were analyzed, all with estimated and the true AM. Three radiologists participated in lesion detection tasks with images reconstructed with both AMs and rated scores for detectability.

Results: The mean relative difference of SUVmean in lesion and normal liver tissue were 3.30 and 6.69 %. The average lesion-to-background contrast (detectability) with delayed PET images using CT AM was 60 % higher than that of the earlier PET image, and was 64 % higher when using the data-based AM. %DSUV for lesions and liver backgrounds with CT-based AM were -0.058 ± 0.25 and -0.33 ± 0.08 while with data-based AM were -0.00 ± 0.26 and -0.28 ± 0.08. Only slight significance difference was found between using CT-based AM and using the data-based AM reconstruction delay phase on %DSUV of lesion. The scores associated with the two AMs matched well consistently.

Conclusions: Our method may be used in delayed PET imaging, which allows no secondary CT radiation in delayed phase. The quantitative analysis for lesion detection purpose could be ensured.

Lifang Pang and Wentao Zhu contributed equally to this work.

Correspondence to: Hongcheng Shi; *e-mail:* shi.hongcheng@zs-hospital.sh.cn

Keywords: Positron emission tomography/computed tomography (PET/CT), Radiation dose, Algorithm

Introduction

Positron emission tomography (PET) has been widely used for staging cancer and therapy response assessment [1, 2]. The PET image represents the accumulated tracer uptake during the acquisition interval, which reflects the metabolism rate of organs and tissues. In clinic, a PET scan for each bed position typically takes 3–5 min for each bed position. The PET data is sorted and reconstructed using image reconstruction algorithms to obtain a PET image. One shortcoming of this routine protocol is that the acquisition time is too short and therefore does not exploit the dynamic change of tracer uptake over time.

One possibility of exploring the temporal change is to perform dynamic imaging, which collects PET data continuously for a long period of time (1–2 h). Dynamic imaging can be used to significantly improve lesion detectability [3, 4]. The major drawback of dynamic imaging is the long scan time, during which patients are required to stay still. The decrease of patient comfort and the low throughput make it undesirable in clinical applications.

Delayed PET imaging (or dual-time-point imaging), on the other hand, has significant advantage over a single PET scan with improved lesion detectability due to the measurement of activity at different acquisition time. It also reduces the total scan time and enables more flexibility by allowing the patients to rest during scans. In literature, Alkhawaldeh et al. found that dual-time-point 2-deoxy-2-[^{18}F]fluoro-D-glucose ([^{18}F]FDG)-PET improves not only the sensitivity and specificity for malignant lung nodules diagnosis but also the diagnostic accuracy relative to single frame standard uptake value (SUV) [5]. Research of Zhuang et al. [6] and Kumar et al. [7] concluded that malignant lesions show a significant increase in SUV over time, while benign lesions show a decrease. In brain lesion studies, Prieto et al. showed that dual-time-point PET improves sensitivity for the identification and volume delineation of high-grade brain tumors compared with standard PET studies [8].

Conventionally, the delayed PET imaging protocol usually includes a secondary PET acquisition 40–60 min after the first PET/x-ray computed tomography (CT) scan [6, 9]. The patients are required to keep rigid between the two acquisitions, so that the matched CT may serve for attenuation correction (AC) for the PET reconstruction of the delayed scan. A possible alternative is allowing patient to leave and performing another PET/CT scan later. However, this approach significantly increases radiation dose because of a secondary CT.

This is exactly a major drawback for delayed imaging, as AC is so critical to quantitative PET image reconstruction. Routinely, transmission scans have been used to compute attenuation map in PET reconstruction [10]. However, some PET scans are without transmission measurements such as in PET/magnetic resonance imaging (MRI) [11], or with an altered protocol (for example, contrast enhanced CT has an elevated Hounsfield unit so cannot be used directly to obtain accurate attenuation coefficients). An even more challenging situation is when no co-registered anatomical images are available; therefore, only the PET data may be used. One way of doing so is to apply the consistency condition [12–15]. The other possibility is to use likelihood optimization and jointly update the attenuation and emission [16], which may be used in PET/MRI and other applications, such as truncated CT image [17], to reduce quantitative error of the reconstructed PET images [18].

However, the theoretical joint estimation algorithms, such as maximum likelihood of activity and attenuation (MLAA) or maximum likelihood of activity and attenuation correction factors estimation (MLACF) [19], have several limitations in application on clinical datasets. One is the undetermined scatter events, which is assumed to be known in the algorithms. In the commonly adopted scatter estimation approach, *i.e.*, single scatter simulation (SSS [20]), attenuation map is required for generating scatter estimation. With unknown attenuation map as well as scatter correction, MLAA would not work properly. The other is the scaling problem, which is necessary to address for absolute PET quantification. This paper focused on the aforementioned problems and proposed practical solutions to synthetically apply the joint estimation on delayed PET imaging.

Materials and Methods

Our clinical study aimed at using the delayed PET images to re-evaluate the patients after initial review of their first PET/CT images and to make more accurate clinical interpretation. The protocol of our study was as follows: the patients first went through whole-body PET/CT scan ~ 1 h after [^{18}F]FDG injection, after which they left the scanner to rest. Then, a second PET/CT scan ~ 2 h post injection of a single bed position (focused on the abdomen) was performed based on the doctor’s interpretation on the initial PET/CT images.

Body Mask Segmentation

Our first step was to segment the body mask for the delayed imaging. It not only led to a more constraint optimization problem by enforcing non-zero update of attenuation coefficients within the body but also ensured a more accurate tail fitting in SSS. Poor initialization might lead to slow convergence and even unstable update.

As no co-registered anatomical images were available, the segmentation was based on PET image of the delayed scan. Without a known attenuation map and scatter estimate, reconstructed PET images may contain images artifacts such as elevated activity out of patient body. These artifacts could reduce segmentation accuracy. We developed an iterative strategy to solve this issue.

Our body mask segmentation method included the following steps: firstly, a time-of-flight (TOF) reconstruction is performed without AC, yet with scatter correction (initially set to zero). A level-set segmentation algorithm is performed upon the reconstructed image to obtain a coarse segmentation of the body. Secondly, construct an initial attenuation map by assigning water attenuation coefficient (0.096/cm) to voxels within the body and air attenuation coefficient (0/cm) out of the body. Estimate a preliminary scatter distribution with SSS and the initial attenuation map from the last step. Repeat all the previous three steps, updating scatter correction in the first step accordingly. In the last "iteration," a TOF reconstruction with the refined AC and the scatter estimation is performed, and a final segmentation is executed upon the reconstructed PET image to obtain the final body mask.

Joint Estimation of Emission, Attenuation, and Scatters

Ideally, the forward projection of the reconstructed image with corrections (attenuation, randoms, scatters, normalization) is supposed to match PET acquisition data in the sinogram space. This may be written as follows:

$$y_i(t) = a_i \sum_j P_{ijt} x_j + r_i(t) + s_i(t) \tag{1}$$

Here, $y_i(t)$ is the number of counts in sinogram for the t-th TOF bin at LOR i, P_{ijt} is the TOF system matrix, x_j is the intensity of the j-th voxel in image,, $s_i(t)$ and $r_i(t)$ are the scatters and randoms estimation for the t-th TOF bin at the i-th LOR, and a_i is the attenuation at LOR i and may be expressed as the following:

$$a_i = e^{-\sum_j l_{ij} \mu_i} \tag{2}$$

where l_{ij} is the length of the i-th line-of-response (LOR) intersecting with voxel j, and μ_i is the attenuation coefficient of the j-th voxel in the attenuation map.

In the iterative joint estimation method, denoting $u_j^{(n,m)}$ as the current estimated attenuation coefficient for voxel j at n-th iteration and m-th subset, the attenuation sinogram can be written as follows:

$$\overline{a}_i^{(n,m)} = e^{-\sum_{j=1}^{J} l_{ij} u_j^{(n,m)}} \tag{4}$$

In the nested joint update, a TOF OSEM reconstruction method [21] is firstly applied to reconstruct the PET image while keeping the attenuation map fixed. The initialization of $s_i(t)$ is computed with SSS and the preliminary AM from section A and is modified in future iterations:

$$f_j^{(n,m+1)} = \frac{f_j^{(n,m)}}{\sum_{t,i \in S_m} \overline{a}_i^{(n,m)} P_{ijt}} \sum_{t,i \in S_m} P_{ijt} \frac{y_i(t)}{\sum_k P_{ikt} f_k^{(n,m)} + \frac{s_i(t) + r_i(t)}{\overline{a}_i^{(n,m)}}} \tag{5}$$

Here, $f_j^{(n,m)}$ is the updating image at n-th iteration and m-th subset.

After updating$f_j^{(n,m)}$, the contribution of the updated emission image in the sinogram space may be computed as the following:

$$\overline{y}_i^{(n,m)} = \overline{a}_i^{(n,m)} \sum_{j,t} P_{ijt} f_j^{(n,m+1)} \tag{6}$$

The following equation is used to update the attenuation coefficients for the AM [16]:

$$\mu_j^{(n,m+1)} = \mu_j^{(n,m)} + \frac{\left. \sum_{i \in S_m} l_{ij} \frac{\overline{y}_i^{(n,m)} \left(\overline{y}_i^{(n,m)} + s_i + r_i - y_i \right)}{\overline{y}_i^{(n,m+1)} + s_i + r_i} - \beta \times \frac{\partial C(\mu)}{\partial \mu_j} \right|_{\mu=\mu^{(n,m)}}}{\left. \sum_{i \in S_m} l_{ij} \frac{\left(\overline{y}_i^{(n,m)} \right)^2}{\overline{y}_i^{(n,m)} + s_i + r_i} \sum_k l_{ik} + \beta \times \frac{\partial^2 C(\mu)}{\partial {\mu_j}^2} \right|_{\mu=\mu^{(n,m)}}} \tag{7}$$

where y_i represents total number of counts at LOR i, s_i and r_i represent non-TOF scatters and randoms estimation at LOR i, and C represents the penalty encouraging attenuation coefficients to converge towards the ones for soft tissue, air, or bone [22, 23]. The major drawback of the non-convex penalty is that the entire cost function would be non-convex and it is possible to "converge" to a local optima. Practically, we carefully chose a good initialization point to encourage the algorithm to converge to somewhere close to the ground truth.

Finally, the update for scatter correction is performed with the updated attenuation map from (7) and the raw PET data, using SSS model. These steps constituting the joint iterative framework for our method may be summarized as follows: first obtain the body boundary mask with segmentation method in section A; secondly, compute scatter correction with SSS and the attenuation map masked by the body boundary; thirdly, run MLAA to update emission image and attenuation map. Then, we update scatter correction estimation with improved attenuation map from the last step. Finally, we repeat the previous steps except the first one and terminate when certain criterion is met.

To address the scaling problem, a regularization operation was applied to guide the convergence towards the correct scaling. Firstly, the 3D body mask was summed slice by slice to generate a 1D axial profile of the body mask for the delayed scan. The profile for the body mask of the whole-body PET/CT scan was acquired in the same way. By shifting the two profiles to allow maximum correlation, the best truncation of the whole-body PET/CT scan for matching the delayed scan was obtained. The truncated CT image (and the truncated AM) now might be a good approximation for the delayed scan, although mismatches did exist due to non-rigid movement. The axial profile for the truncated AM was then used to enforce the update of the AM yielding the same axial profile. This simple solution, although preliminary, behaved quite well in addressing the scaling problem.

Subject Demographics

Fourteen patients (11M/3F) with suspected liver lesions were included in the study. The mean age of these 14 patients was 56.1 ± 9.2 years, ranging from 34 to 68 years. A written informed consent form was obtained for each subject. This research was approved by the Institutional Review Board of Zhongshan Hospital of Fudan University.

PET/CT Acquisition

PET/CT data was collected on uMI510 PET/CT system manufactured by Shanghai United Imaging Healthcare. The uMI510 PET/CT scanner combines a 96-ring LYSO PET with a 16-slice CT tomography. The PET system has a total of 24 modules and each block is formed with 16 × 16 crystals (2.35 mm × 2.35 mm × 15 mm). This configuration has a 236 mm axial and 700 mm transverse reconstruction field-of-view (FOV). The system has a 480-ps timing resolution. The coincidence data was acquired in list mode format and then processed by a fully 3D attenuation-weighted ordered subset expectation maximization OSEM (3D AW-OSEM) with all necessary corrections. All patients fasted for at least 6 h before examination. The serum glucose just before PET/CT scanning was less than 10 mmol/dl. Patients were scanned at 50–60 min after the intravenous (i.v.) injection of [^{18}F]FDG (4.44 MBq/kg), typically, patients were scanned from the base of the skull to the mid-thigh. Acquisition time was 3 min per table position. The delayed scan was performed ~60 min after the whole-body scan finished. The scanning part was on the abdomen including the liver and the acquisition time was 3 min per table position. All raw and processed data were inspected and verified to be of good quality for analysis.

Quantitative Analysis

ROIs were drawn in multiple locations in the whole-body PET images as well as the delayed PET images reconstructed with the CT-based AM and the estimated AM for each patient. SUVmean and SUVmax were computed. Lesion detectability was numerically computed as the ratio of lesion SUVmax and normal liver tissue SUVmax. %DSUV (percentage change of SUVmean at two different time points) was computed according to the formula $\%DSUV = (SUV_{delay} - SUV_{early}) / SUV_{early}$ where SUV_{early} and SUV_{delay} were SUVmean for the early and delayed PET scan, respectively.

Three radiologists reviewed the delayed PET images reconstructed with the CT-based AM and PET data-based AM in a blind review and were asked to rate a score 1–5 for the lesion detectability in the two delayed PET images. In rating score, 1 meant not identifiable, 2 was difficult to identify, 3 was modestly identifiable, 4 was easy to identify, and 5 was surely identifiable.

Statistical Analysis

All statistical analyses were performed with SPSS (SPSS for Windows, version 19.0; SPSS Inc) and MATLAB software (R2015a). The numerical values were expressed in mean ± SD. The value of SUVmax and the %DSUV of two groups were compared using paired *t* test. Differences were considered significant when $P < 0.05$.

Results

The PET data-based segmentation method was evaluated by comparing the segmented body mask with the CT-based body mask for the delayed scan. Let I(seg) represent a binary image with value = 1 for voxels inside segmented body and value = 0 otherwise. Let I(CT) represent the binary image with value = 1 for voxels inside body region recognized from CT and value = 0 otherwise. Relative correlation was computed to measure the similarity between I(seg) and I(CT). Figure 1 is exemplary views of the CT-based mask, data-based mask, and their difference.

The body mask was critical for stabilizing the algorithm and maintaining correct AM topography. In practice, it was found that algorithm without this mask information resulted in attenuation maps much larger than the ground truth, *i.e.*, non-zero attenuation coefficients were out of the patient body, causing apparent artifacts of the AM and quantitative bias of the emission image.

Figure 2 shows an example of the estimated attenuation maps with our method, the ground truth attenuation map computed from the delayed CT image, and their difference. Due to the limited counts for the delayed scan, the algorithm was terminated after 6 iterations to avoid high noise in the reconstructed image. Therefore, the recovery of attenuation

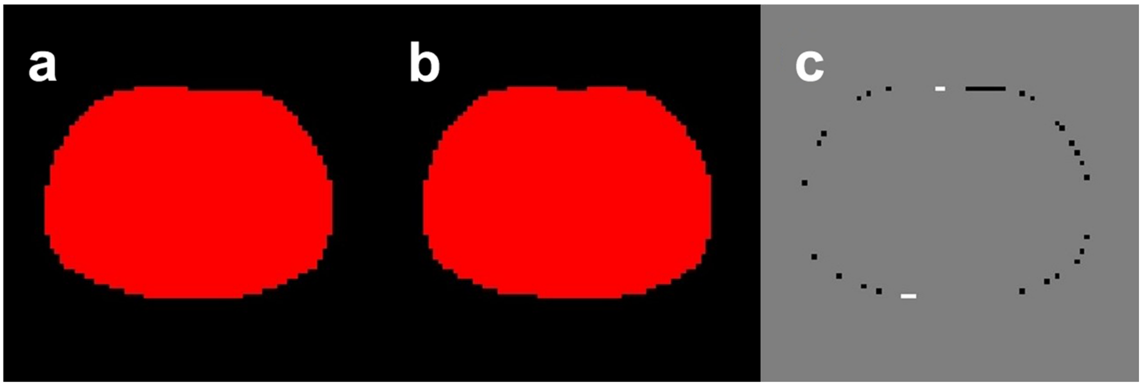

Fig. 1. **a** Exemplary segmented body masks of the CT-based method, **b** the PET data-based method, and **c** the difference. The masks are exhibited as binary images. The mask image matrix is 127 × 127 × 97 with voxel size 4.88 × 4.88 × 2.44.

coefficients in several regions especially in the spine was not ideal and may have ~ 5 % error.

To make comparison, PET images were reconstructed with ordered subset expectation maximization (OSEM) with 3 TOF iterations and 20 subsets, after obtaining the estimated AM and the CT-based AM. Normalization, attenuation, random correction, and scatter correction were applied. Figure 3 shows an example of the reconstructed delayed PET images with the estimated AM, the CT-based AM, and their difference. The two reconstructed PET images were qualitatively and quantitatively quite similar. The maximum SUV difference was found to be in the spine, which had a relative difference < 10 % for almost all the datasets (only one patient has ~ 12 % relative difference). For soft tissues with attenuation coefficients close to 0.096/cm, the SUV difference was usually much lower.

To explore the potential of dual-time point imaging (earlier scan + delayed scan), the earlier PET image was reconstructed also using OSEM with 3 TOF iterations and 20 subsets. The attenuation correction was computed from the co-registered CT image in the early scan. ROIs in lesions and background tissue of same volume in approximately same locations as in the delayed scans were carefully drawn in the earlier PET images.

A total of 24 liver lesions were detected in the [^{18}F]FDG PET/CT imaging of the 14 patients. Pathologically, five lesions were hepatocellular carcinomas, five lesions were metastatic adenocarcinoma of liver from colorectal cancer, while there were two cholangiocarcinomas, two reactive hyperplasia of liver lymphatic tissue, and one hilar cholangitis confirmed by surgery. Four lesions were suspected hepatocellular carcinomas while five lesions were suspected metastatic tumors from gastrointestinal tract which was confirmed by CT or MRI imaging. The clinical and demographic information of the 14 patients with 24 liver lesions was shown in Table 1.

SUVs of the early (reconstructed with early CT-based AM) and delayed (reconstructed with the CT-based AM and PET data-based AM both) PET images were shown in Tables 2, 3, and 4. For each patient, ROIs were carefully drawn in normal liver tissues as well as in lesions in the earlier and delayed PET images by the radiologists. The ROIs in the lesions were drawn according to the size identified in the CT image. The ROIs in normal liver tissues were drawn with at least 5 ml volume in a uniform background. SUVmean and SUVmax were computed in each ROI. For each metric, the relative difference of using two AMs was computed from Tables 3 and 4. The mean relative difference of SUVmean in lesion and normal liver

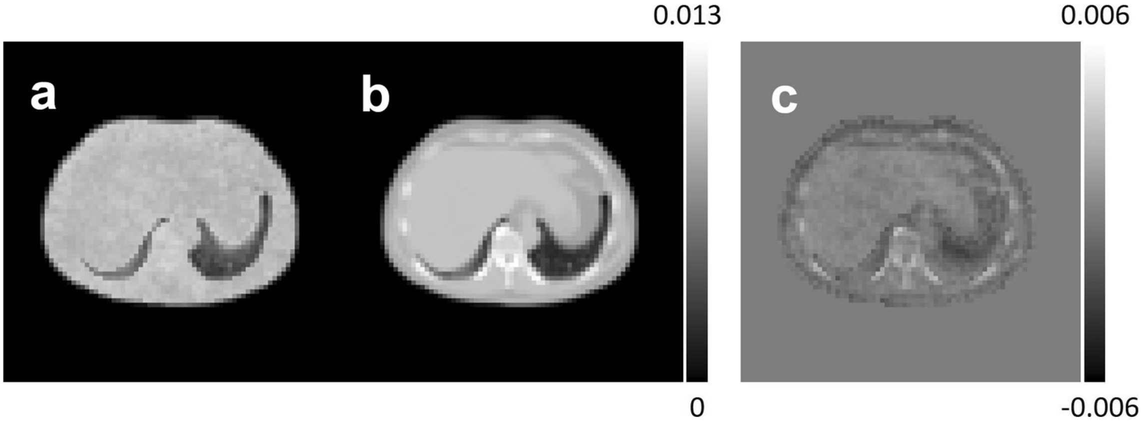

Fig. 2. **a** estimated attenuation map, **b** CT-based attenuation map, and **c** difference between **b** and **a**. These images are 127 × 127 × 97 with voxel size 4.88 × 4.88 × 2.44.

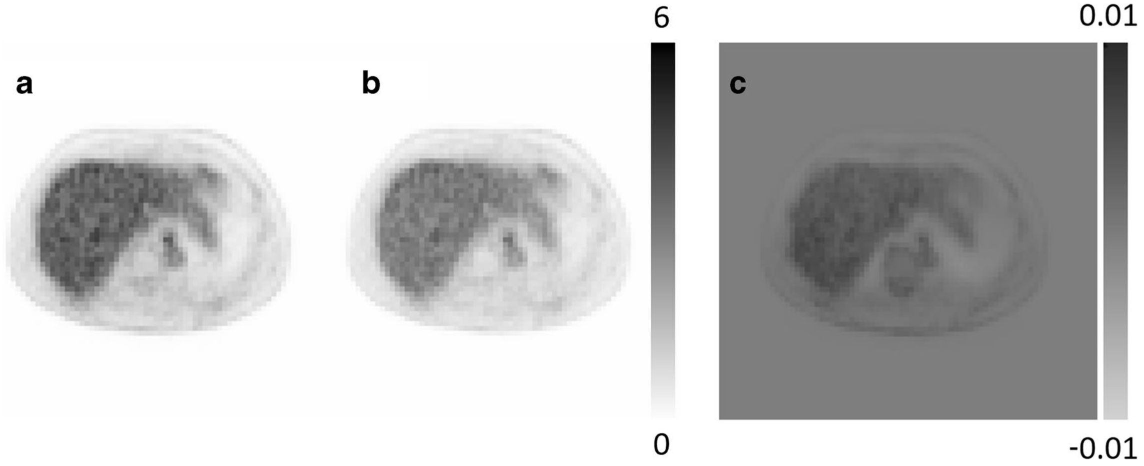

Fig. 3. Transverse view of the PET activity images reconstructed with **a** true attenuation map **b** estimated attenuation map, **c** is the difference image of a and b. These images are 127 × 127 × 97 with voxel size 4.88 × 4.88 × 2.44.

tissue were 3.30 and 6.69 %. These relative differences were not quite significant and indicated that the proposed method could generate attenuation maps with high accuracy and yielded quite small quantitative error in SUV in the reconstructed PET images.

The lesion detectability was numerically measured by the activity contrast of lesion against normal liver background, which is computed as the ratio of respective SUVmax. The lesion-tissue contrast for all lesion detection tasks were summarized in Fig. 4. For the delayed imaging, the performance with two inputs (red and green points in Fig. 4) turned out to be quite consistent. The mean of relative difference was 2.53 %. For just a few lesions, the detectability had significant difference. This might be because of the crosstalk of emission and attenuation in running joint estimation which led to elevated activity in using the data-based AM. Besides, the detectability of delayed PET imaging was almost consistently higher than that of the earlier PET images. The average detectability with delayed PET images using CT AM was 60 % higher than that of the earlier PET image, and was 64 % higher when using the data-based AM. Only one ROI (#9) had lower detectability with delayed PET images.

To explore the benefit of delayed PET imaging, %DSUV was computed based on the SUVmean of the earlier and later scan to represent the percentage change of SUV over

Table 1. Clinical and demographic information of the 14 patients with 24 liver lesions

Patient number	Gender	Age	Lesion number	Lesion size (mm)	Histology
1	F	64	1	37.8 × 34.8	Intrahepatic cholangiocarcinoma
2	F	47	2	11.8 × 10.6	Hilar cholangiocarcinoma
3	M	68	3	79.6 × 46.9	HCC, II ~ III
			4	57.8 × 44.2	HCC, II ~ III
4	M	58	5	32.6 × 27.6	HCC, II ~ III
5	M	58	6	32.3 × 26.2	HCC, III
			7	16.9 × 15.4	HCC, III
6	M	44	8	70.2 × 91.5	Suspect HCC
7	M	53	9	14.7 × 14.1	Suspect HCC
			10	20.7 × 12.5	Suspect HCC
8	M	66	11	35.7 × 30.0	Suspect HCC
9	M	62	12	21.8 × 21.7	Suspect Hepatic metastases
			13	12.6 × 12.6	Suspect Hepatic metastases
10	F	58	14	20.1 × 12.7	Suspect Hepatic metastases
			15	12.1 × 7.4	Suspect Hepatic metastases
			16	12.4 × 8.4	Suspect Hepatic metastases
11	M	54	17	20.2 × 17.4	Hepatic metastases
12	M	34	18	9.4 × 9.0	Hepatic metastases
			19	8.4 × 8.7	Hepatic metastases
			20	10.2 × 7.4	Hepatic metastases
			21	6.1 × 5.2	Hepatic metastases
13	M	60	22	17.6 × 10.8	cholangitis
14	M	59	23	17.5 × 11.4	RHLL
			24	18.5 × 13.9	RHLL

HCC hepatocellular carcinoma, *RHLL* reactive hyperplasia of liver lymphatic tissue

Table 2. SUVs for corresponding ROIs in the early PET/CT scan of the 14 patients with 24 liver lesions

Lesion number	Lesion SUVmean	Lesion SUVmax	Liver SUVmean	Liver SUVmax	SUVmax ratio
1	6.97	19.66	2.43	2.91	6.76
2	4.05	7.69	2.74	3.2	2.40
3	3.36	10.07	2.54	3.79	2.66
4	3.79	7.66	2.54	3.79	2.02
5	2.62	5.08	2.07	2.64	1.92
6	3.53	6.49	2.10	2.82	2.30
7	3.97	5.72	2.10	2.82	2.03
8	4.55	12.77	2.55	3.55	3.60
9	3.09	6.26	2.28	3.12	2.01
10	3.83	7.97	2.28	3.12	2.55
11	3.04	4.38	2.38	2.94	1.49
12	4.87	7.72	1.94	2.87	2.69
13	3.93	6.27	1.94	2.87	2.18
14	2.49	4.45	2.05	2.33	1.91
15	3.31	6.00	2.05	2.33	2.58
16	3.77	4.96	2.05	2.33	2.13
17	5.11	15.69	2.08	3.18	4.93
18	3.43	5.18	2.13	2.47	2.10
19	3.62	5.54	2.13	2.47	2.24
20	4.1	6.72	2.13	2.47	2.72
21	2.86	4.41	2.13	2.47	1.79
22	3.98	8.07	2.06	2.52	3.20
23	3.56	5.13	2.31	2.76	1.86
24	3.93	7.4	2.31	2.76	2.68

SUVmax ratio was defined as the ratio of SUVmax of lesion and SUVmax of background liver

two acquisition time points. Two versions of %DSUV were computed associated with two different AMs. %DSUV for lesions and liver backgrounds with CT-based AM were -0.05 ± 0.25 and -0.33 ± 0.08. %DSUV for lesions and liver backgrounds with data-based AM were -0.00 ± 0.26 and -0.28 ± 0.08. It was quite clear that the contrast of %DSUV between the lesion and background was quite significant. Also there was only slight significance difference between using CT-based AM and using the data-based AM reconstruction delay phase on %DSUV of lesion ($P = 0.04$). There was significant difference on %DSUV of surgically conformed or suspected HCC lesion between using CT-based AM and using the data-based AM reconstruction delay phase ($P = 0.01$). While there was no significant difference between using CT-based AM and using the data-based AM reconstruction delay phase on %DSUV of surgically conformed or suspected hepatic metastases lesions ($P = 0.29$). Performing dual-time-point imaging analysis thus suffered from negligible bias if the data-based AM was used to replace the CT-based AM.

The scores for all lesion detection tests were reported in Fig. 5. Generally, the scores associated with the two AMs matched well consistently. There were six tests where using the data-based AM were 1 point higher, possibly because of elevated AC due to crosstalk.

Table 3. SUVs for corresponding ROIs in the delayed PET images reconstructed with CT-based AM. All ROIs corresponded to the ROIs drawn in the early PET anatomically of the 14 patients

Lesion number	Lesion SUVmean	Lesion SUVmax	Liver SUVmean	Liver SUVmax	SUV max ratio	Detection score
1	7.89	20.92	1.95	2.61	8.02	4
2	2.21	6.23	1.43	1.89	3.30	4
3	3.08	10.29	1.81	2.06	5.00	4
4	2.36	5.38	1.81	2.06	2.61	3
5	2.01	2.86	1.32	1.53	1.87	3
6	3.96	8.23	1.51	1.97	4.18	4
7	3.55	7.02	1.58	2.06	3.41	5
8	5.65	13.80	1.32	1.59	8.68	5
9	3.42	6.86	1.58	1.89	3.63	4
10	3.52	7.01	1.58	1.89	3.71	4
11	1.49	2.19	1.72	1.95	1.12	3
12	5.82	10.25	1.2	1.63	6.29	4
13	4.42	9.48	1.2	1.63	5.82	4
14	3.31	4.59	1.38	1.49	3.08	4
15	2.77	4.08	1.48	1.57	2.60	4
16	2.51	3.56	1.39	1.79	1.99	4
17	5.47	13.88	1.41	1.75	7.93	5
18	2.54	3.93	1.46	1.67	2.35	5
19	4.98	7.21	1.35	1.75	4.12	5
20	4.19	8.65	1.48	1.67	5.18	4
21	1.92	2.85	1.47	1.67	1.71	4
22	5.22	13.12	1.78	2.08	6.31	4
23	3.08	5.24	1.26	1.59	3.30	5
24	3.48	7.16	1.41	1.61	4.45	5

SUVmax ratio was defined as the ratio of SUVmax of lesion and SUVmax of background liver. Detection score was rated by the physicians according to their visual interpretation of lesion detectability

Table 4. SUVs for corresponding ROIs in the delayed PET image reconstructed with data-based AM (MLAA). All ROIs corresponded to the ROIs drawn in the early PET anatomically

Lesion number	Lesion SUVmean	Lesion SUVmax	Liver SUVmean	Liver SUVmax	SUV max ratio	Detection score
1	6.22	23.05	2.1	2.97	7.76	4
2	2.4	7.04	1.62	2.07	3.40	4
3	3.78	11.62	2.1	2.39	4.86	4
4	2.71	6.79	2.25	2.61	2.60	4
5	2.58	4.26	1.42	1.78	2.39	3
6	4.09	8.01	1.5	1.81	4.43	5
7	4.09	8.13	1.54	1.82	4.47	5
8	5.68	14.18	1.52	1.74	8.15	5
9	3.56	7.58	1.73	2.19	3.46	4
10	3.73	8.61	1.73	2.19	3.93	4
11	1.48	2.30	1.78	2.18	1.06	3
12	5.26	10.82	1.23	1.68	6.44	5
13	4.56	10.59	1.23	1.68	6.30	5
14	3.59	5.34	1.4	1.74	3.07	4
15	2.37	4.98	1.5	1.85	2.69	4
16	2.97	4.01	1.58	1.73	2.32	4
17	5.5	14.67	1.49	1.82	8.06	5
18	2.67	4.09	1.38	1.94	2.11	5
19	5.36	7.95	1.52	1.72	4.62	5
20	4.88	10.17	1.57	1.99	5.11	5
21	1.91	2.84	1.49	1.67	1.70	5
22	5.47	14.13	1.66	2.09	6.76	4
23	2.99	5.06	1.47	1.81	2.80	5
24	3.93	8.23	1.47	1.67	4.93	5

SUVmax ratio was defined as the ratio of SUVmax of lesion and SUVmax of background liver. Detection score was rated by the physicians according to their visual interpretation of lesion detectability

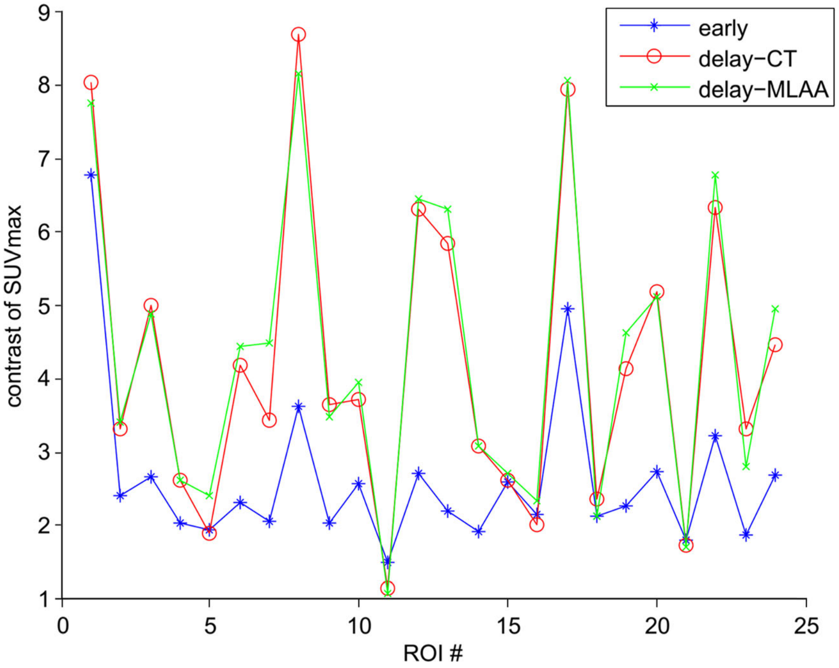

Fig. 4. The lesion-tissue contrast of a total of 24 ROIs for the patients in this study. The contrast was computed as ratio of SUVmax in lesion ROIs to SUVmax in normal liver tissue ROIs.

Discussion

Practically, the application of joint estimation (such as MLAA) is limited by several factors. MLAA is known to determine the attenuation map up to a constant [24]. Therefore, the scaling problem needs to be solved for absolute quantification. On the other hand, some literature regularized the optimization function [25, 26] by encouraging the AM values to converge towards the attenuation coefficients of soft tissue, bone, and air. Consequently, the problem was transformed to a non-convex problem with difficult-to-tune parameters. The method proposed in this paper applied a scaling technique encouraging the method to provide reasonable results. Empirically, we found that it worked well without visible divergence from the "ground truth." In the future, further modification may be made upon the current solution.

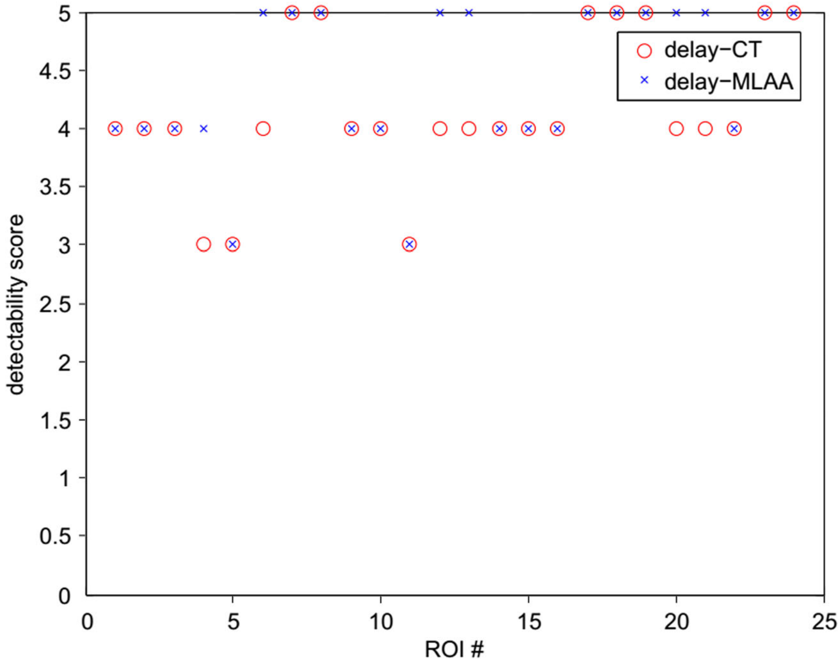

Fig. 5. The lesion detectability scores rated by three radiologists in the blind review for the two input AMs.

Another fundamental requirement for the joint estimation algorithm to work well is that TOF and non-TOF reconstructed images have to be quantitatively consistent, which is subject to many factors. On the one hand, TOF reconstruction is less sensitive than non-TOF one to errors of correction terms [21]. The bias of data correction terms such as scatter, random, and normalization estimation could cause significant artifacts and quantitative errors. Among those, scatter estimation may be the most difficult one to address. The widely used scatter estimation method: SSS, only models single scattered events and neglects multiple scattered events. For large patient, the scatter fraction as well as the percentage of multiple scatters in total scatter events increases dramatically and therefore using the SSS model incurs more and more significant errors. Furthermore, out of FOV scatter events are difficult to estimate because the data acquisition is constraint to the current bed position only and no information out of the FOV is available. Although direct Monte Carlo-based scatter compensation approaches [27] has been shown to bring some improvement, the excessive high computation cost is not practical for routine clinical scans. On the other hand, TOF PET data is more sensitive and volatile. TOF system is subject to timing drift of coincidences. Therefore, an event might be mistakenly classified to the neighboring TOF bin when sorting the data according to the TOF information. Therefore, inconsistencies could easily exist between TOF and non-TOF reconstructions, which influence the accuracy of MLAA. These practical issues will all need further attention for the joint estimation algorithm to have better performance.

Patient body deformation is a major challenge for delayed imaging, even for patients without active motion during two data acquisitions. This is because non-rigid organ motion within the body is inevitable. For example, researchers have shown that liver is an organ easily subject to deformation during scan [28, 29]. Therefore, using CT associated with the first PET acquisition for attenuation correction purpose of the second PET acquisition is inaccurate and may cause artifacts in the reconstructed PET image. If one wants to use the first CT, one solution is to warp the CT image according to the deformation field obtained by image registration [30, 31] between the two acquisitions, so that the deformed CT can serve for attenuation correction for the delayed PET scan [32]. However, with standard techniques, the deformation field is difficult to obtain because the registration has to be performed between the first PET (or CT) image and the delayed PET image. Without proper AC and scatter correction, the delayed PET image turns out to have low quality for image registration. Our method obviates this challenging registration requirement by following the joint estimation framework and directly estimating the delayed AM from the PET data [16]. We also built our mask and scaling solutions upon methods proposed by researchers in literature [33, 34]. Practically, we may further improve the performance of our method by running a registration between the first CT-computed attenuation map and the estimated attenuation map after the joint estimation algorithm is terminated. This registration is usually more robust as these two attenuation maps are with "same modality" and have quite similar values.

Conclusions

To conclude, a PET data-driven joint estimation method for delayed PET imaging was proposed in this paper. Several challenges such as scatter correction estimation and scaling problem were addressed with practical solutions. The quantification of the delayed PET image as well as the dual-time-point analysis was accurately maintained when the proposed method was used.

Acknowledgments. Funding support from the National Nature Science Foundation of China (81671735), the National Key Research and Development Program of China (2016YFC0103908), and Program of Ministry of Science and Technology of Shanghai (17511104201) is gratefully appreciated.

Compliance with Ethical Standards

Conflicts of Interest Statement

The authors declare that they have no conflict of interest.

References

1. Antoch G, Stattaus J, Nemat AT, Marnitz S, Beyer T, Kuehl H, Bockisch A, Debatin JF, Freudenberg LS (2003) Non-small cell lung cancer: dual-modality PET/CT in preoperative staging. Radiology 229:526–533
2. Wahl RL, Quint LE, Greenough RL, Meyer CR, White RI, Orringer MB (1994) Staging of mediastinal non-small cell lung cancer with FDG PET, CT, and fusion images: preliminary prospective evaluation. Radiology 191:371–377
3. Anzai Y, Minoshima S, Wolf GT, Wahl RL (1999) Head and neck cancer: detection of recurrence with three-dimensional principal components analysis at dynamic FDG PET. Radiology 212:285–290
4. Zhu W, Li Q, Bai B, Conti PS, Leahy RM (2014) Patlak image estimation from dual time-point list-mode PET data. IEEE Trans Med Imaging 33:913–924
5. Alkhawaldeh K, Bural G, Kumar R, Alavi A (2008) Impact of dual-time-point ^{18}F-FDG PET imaging and partial volume correction in the assessment of solitary pulmonary nodules. Eur J Nucl Med Mol Imaging 35:246–252
6. Zhuang H, Pourdehnad M, Lambright ES, Yamamoto AJ, Lanuti M, Li P, Mozley PD, Rossman MD, Albelda SM, Alavi A (2001) Dual time point ^{18}F-FDG PET imaging for differentiating malignant from inflammatory processes. J Nucl Med 42:1412–1417
7. Kumar R, Loving VA, Chauhan A, Zhuang H, Mitchell S, Alavi A (2005) Potential of dual-time-point imaging to improve breast cancer diagnosis with ^{18}F-FDG PET. J Nucl Med 46:1819–1824
8. Prieto E, Martí-Climent JM, Domínguez-Prado I et al (2011) Voxel-based analysis of dual-time-point ^{18}F-FDG PET images for brain tumor identification and delineation. J Nucl Med 52:865–872
9. Kubota K, Itoh M, Ozaki K, Ono S, Tashiro M, Yamaguchi K, Akaizawa T, Yamada K, Fukuda H (2001) Advantage of delayed whole-body FDG-PET imaging for tumour detection. Eur J Nucl Med Mol Imaging 28(6):696–703
10. Kinahan PE, Hasegawa BH, Beyer T (2003) X-ray-based attenuation correction for positron emission tomography/computed tomography scanners. Semin Nucl Med 33:166–179
11. Shao Y, Cherry SR, Farahani K, Meadors K, Siegel S, Silverman RW, Marsden PK (1997) Simultaneous PET and MR imaging. Phys Med Biol 42:1965–1970

12. Panin VY, Kehren F, Hamill JJ, Michel C (2004) Application of discrete data consistency conditions for selecting regularization parameters in PET attenuation map reconstruction. Phys Med Biol 49:2425–2436
13. Bronnikov AV (2000) Reconstruction of attenuation map using discrete consistency conditions. IEEE Trans Med Imaging 19:451–462
14. Natterer F (1993) Determination of tissue attenuation in emission tomography of optically dense media. Inverse Probl 9:731–736
15. Natterer F. (1986) The Mathematics of Computerized Tomography. B.G. Teubner. 107–108
16. Rezaei A, Defrise M, Bal G, Michel C, Conti M, Watson C, Nuyts J (2012) Simultaneous reconstruction of activity and attenuation in time-of-flight PET. IEEE Trans Med Imaging 31:2224–2233
17. Hsieh J, Chao E, Thibault J, Grekowicz B, Horst A, McOlash S, Myers TJ (2004) A novel reconstruction algorithm to extend the CT scan field-of-view. Med Phys 31:2385–2391
18. Nuyts J, Bal G, Kehren F, Fenchel M, Michel C, Watson C (2013) Completion of a truncated attenuation image from the attenuated PET emission data. IEEE Trans Med Imaging 32:237–246
19. Nuyts J, Rezaei A, Defrise M (2012) ML-reconstruction for TOF-PET with simultaneous estimation of the attenuation factors. In: Nuclear science symposium and medical imaging conference (NSS/MIC). IEEE:2147–2149
20. Watson CC, Newport D, Casey ME (1996) A single scatter simulation technique for scatter correction in 3D PET. In: Three-dimensional image reconstruction in radiology and nuclear medicine. Springer, pp255–268
21. Conti M (2011) Why is TOF PET reconstruction a more robust method in the presence of inconsistent data? Phys Med Biol 56:155–168
22. Mehranian A, Zaidi H, Reader AJ (2017) MR-guided joint reconstruction of activity and attenuation in brain PET-MR. NeuroImage 162:276–288
23. Bal G, Kehren F, Bao J et al (2013) Maximum likelihood reconstruction of attenuation and activity (MLAA) based extended mu-maps for dynamic and gated MR-PET [abstract]. J Nucl Med 54:Supplement:2
24. Defrise M, Rezaei A, Nuyts J (2012) Time-of-flight PET data determine the attenuation sinogram up to a constant. Phys Med Biol 57:885–899
25. Mehranian A, Zaidi H (2014) MR constrained simultaneous reconstruction of activity and attenuation maps in brain TOF-PET/MR imaging. EJNMMI Phys 1:A55
26. Michel CJ, Nuyts J (2013) Completion of truncated attenuation maps using maximum likelihood estimation of attenuation and activity (MLAA). (USA) US8620053
27. Zaidi H (2000) Comparative evaluation of scatter correction techniques in 3D positron emission tomography. Eur J Nucl Med Mol Imaging 27:1813–1826
28. Vogel WV, Van Dalen JA, Wiering B et al (2007) Evaluation of image registration in PET/CT of the liver and recommendations for optimized imaging. J Nucl Med 48:910–919
29. van Dalen JA, Vogel W, Huisman H et al (2004) Accuracy of rigid CT–FDG-PET image registration of the liver. Phys Med Biol 49:5393–5405
30. Hill DLG, Batchelor PG, Holden M, Hawkes DJ (2001) Medical image registration. Phys Med Biol 46:1–45
31. Rueckert D, Schnabel JA (2010) Medical image registration. In: Deserno TM (ed) Biomedical image processing. Springer press, Berlin, pp 131–154
32. Rezaei A, Michel C, Casey ME, Nuyts J (2016) Simultaneous reconstruction of the activity image and registration of the CT image in TOF-PET. Phys Med Biol 61:1852–1874
33. Heußer T, Rank CM, Freitag MT et al (2016) MR-consistent simultaneous reconstruction of attenuation and activity for non-TOF PET/MR. IEEE Trans Nucl Sci 63:2443–2451
34. Boellaard R, Hofman MB, Hoekstra OS, Lammertsma AA (2014) Accurate PET/MR quantification using time of flight MLAA image reconstruction. Mol Imaging Biol 16:469–477